Inorganic Chemistry

pubs.acs.org/IC

Article

Measurement of Line Width and Anisotropy in C_3/C_4-Symmetric Gd(III) Complexes

Edward Latham, Chowan Ashok Kumar, Carlson Alexander, Nicholas Cox, Thierry Dubroca, David Parker, and Nicholas F. Chilton*

Cite This: *Inorg. Chem.* 2026, 65, 13807−13816

Read Online

ACCESS | Metrics & More | Article Recommendations | Supporting Information

ABSTRACT: Gadolinium(III) complexes are frequently used as spin labels in high-field electron paramagnetic resonance spectroscopy and dynamic nuclear polarization nuclear magnetic resonance spectroscopy due to their high spin ($S = 7/2$) ground state and chemical robustness. A primary goal in their design is to minimize the magnetic resonance line width by engineering the zero-field splitting (ZFS). Here, we present a comprehensive experimental study of a series of C_3-symmetric TPATCN and C_4-symmetric DOTA derivatives. Using multifrequency EPR spectroscopy (34 to 390 GHz) here we try to understand trends in their ZFS parameters (D, E) and their distributions (D_{strain}, E_{strain}). We find that functionalization of the TPATCN scaffold with an electron-withdrawing nitro group (NO_2) minimizes the axial ZFS to $D = 0.0110$ cm^{-1}||0.330 GHz, but this is coupled with a significant increase in conformational flexibility, resulting in a large D_{strain}. Conversely, amide-functionalized DOTA compounds demonstrate superior structural rigidity, evidenced by near-zero rhombic ZFS and small E_{strain}. Many complexes studied herein show considerably smaller resonance line widths than existing tags, suggesting there is scope for the design of improved Gd(III) spin labels.

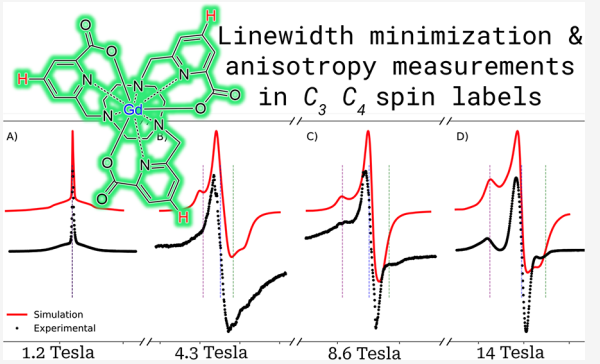

INTRODUCTION

Pulsed electron paramagnetic resonance (EPR) spectroscopy, particularly double electron−electron resonance (DEER), also known as pulsed electron double resonance (PELDOR), has become an indispensable tool for measuring nanometer-scale distance distributions in proteins using site-directed spin labeling (SDSL).[1−3]

Determination of protein distance distributions with DEER/PELDOR has been dominated by spin labels based on nitroxide radicals.[1] However, their utility is severely hampered in physiological settings due to their rapid reduction to EPR-silent species within the cellular milieu, limiting the feasibility of in-cell structural studies.[4,5]

Other uses of spin probes include techniques such as dynamic nuclear polarization (DNP), nuclear magnetic resonance (NMR, sometimes DNP-NMR), which leverage paramagnetic centers to dramatically enhance the sensitivity, a process that also benefits from polarizing agents with narrow EPR line widths.[6,7]

This instability has spurred the development of new classes of spin labels, where Gd(III) complexes have emerged as a superior alternative,[5,8,9] a methodology notably advanced by Goldfarb and Otting.[10] Gd(III) complexes offer remarkable chemical stability in reducing environments and provide significant gains in sensitivity, particularly at high magnetic fields, due to their large spin quantum number $S = 7/2$ compared to the $S = 1/2$ of a nitroxide radical, making them ideal probes for in-cell EPR and high-precision distance measurements.[8,11,12]

Unlike nitroxides, the sensitivity of these high-spin labels is intrinsically linked to the sharpness of the central transition, making line width optimization the foremost design parameter for these tags.[8,13,14]

The Gd(III) ion possesses a half-filled 4f electron shell, resulting in a high-spin $S = 7/2$ ground state with a nearly isotropic g-matrix.[5,13,15] For ions with $S > 1/2$, the spin sublevels experience a splitting even in the absence of an external magnetic field, known as zero-field splitting (ZFS).[16,17] This ZFS lifts the degeneracy of the eight m_S sublevels, causing the total EPR signal intensity to be distributed over seven allowed transitions. Crucially, the central transition between the $m_S = -1/2$ and $m_S = +1/2$ states is not affected by the ZFS to first order, making it significantly sharper and more intense than the other transitions, and thus the primary resonance of interest for

Received: February 2, 2026
Revised: June 4, 2026
Accepted: June 9, 2026
Published: June 15, 2026

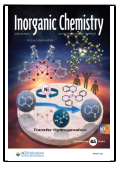

https://doi.org/10.1021/acs.inorgchem.6c00631
Inorg. Chem. 2026, 65, 13807−13816

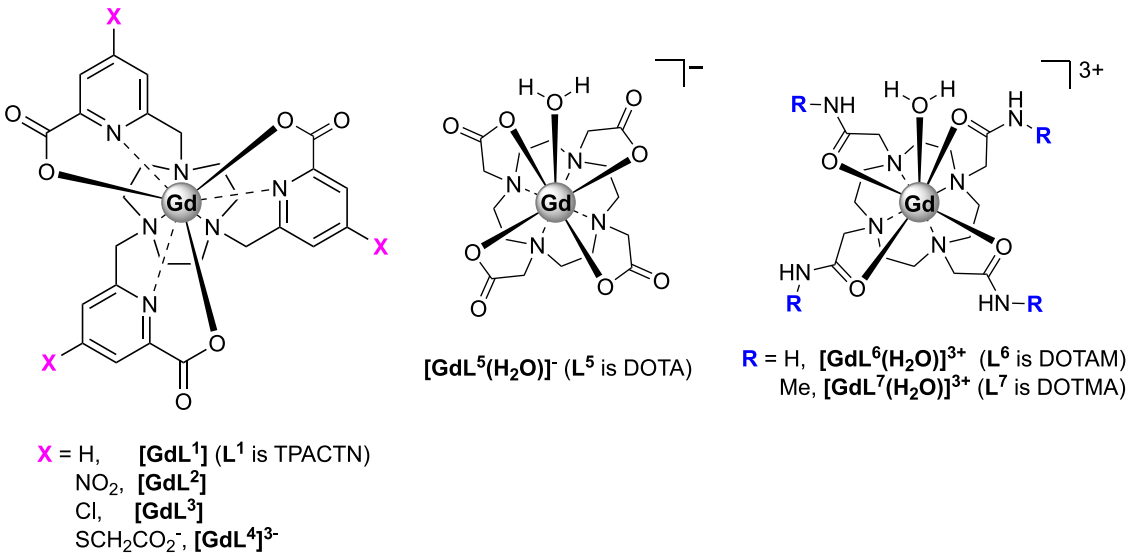

Figure 1. Skeletal structures of the Gd(III) complexes. TPATCN derivatives are shown on the first row, DOTA derivatives follow on the bottom row.

pulsed EPR experiments. The ZFS arises from the interaction of the electron spin with the electrostatic field generated by the coordinating ligands, mediated by second-order spin−orbit coupling.[18,19] It is usually described by the axial (D) and rhombic (E) ZFS parameters, which quantify the deviation of the ligand field from perfect cubic.[16,20] While the ZFS for Gd(III) can be in the GHz range, a coordination environment of high symmetry, such as the approximately C_4 or C_3 environments provided by DOTA (H_4DOTA = 1,4,7,10-tetraazacyclododecane-1,4,7,10-tetraacetic acid) or TPATCN (H_3TPATCN = 1,4,7-tripicolinic acid-1,4,7-triazacyclononane) derivatives, respectively, significantly reduces the magnitude of the D and E parameters.[11,18] Hence, design of the chelating ligand is paramount to optimizing the performance of Gd(III) spin labels. However, while minimizing the crystal-field parameters is our primary spectroscopic objective, the rational design of effective probes must balance electronic requirements with practical constraints; namely, the complex must maintain a compact steric footprint to avoid perturbing the target biomolecule's native structure, retain high aqueous solubility, and possess accessible functional groups for site-selective bioconjugation.

Early examples, such as $[Gd(DTPA)]^{2-}$ (DTPA = diethylenetriamine pentaacetate), exhibit a relatively large ZFS ($D \approx 0.0480$ cm^{-1}‖1.44 GHz), which broadens the transitions out to 5.89 mT at 64 GHz. However, this can be reduced to 0.88 mT at 932 GHz[15] where only the $m_S = +1/2$ and $m_S = -1/2$ states are probed. The widely used $[Gd(DOTA)(H_2O)]^-$ tag has a more moderate ZFS ($D \approx -0.0238$ cm^{-1}‖−0.714 GHz),[14,18] and shows a correspondingly narrower central transition, with a reported line width of just 0.52 mT at 240 GHz, a direct result of the more symmetric coordination environment provided by the C_4 DOTA macrocycle.[21] Therefore, recent efforts have focused on creating highly symmetric coordination environments to minimize the ZFS. The benchmark example is $[GdL^4]^{3-}$ (Figure 1), which is reported to have an exceptionally small ZFS ($D \approx 0.0162$ cm^{-1}‖0.486 GHz) and a very narrow intrinsic line width of approximately 0.5 mT at 240 GHz.[13,18] The success of this example stems from conformationally rigid C_3-symmetric triazacyclononane backbone, which enforces a near-perfect trigonally symmetric coordination of the donor atoms. However, it is clear that the core symmetry of the ligand scaffold is not the only factor influencing the ZFS. This raises a key question: how do electronic modifications to a symmetric ligand framework, such as the introduction of electron-withdrawing or donating groups, affect the ZFS and the resulting EPR line width? Answering this question is the primary motivation for the present study. Note: While we aim to minimize line widths through ligand symmetry, we recognize that determining the exact line shape in a functional context is complex. Protein conjugation introduces site-specific conformational distributions that lower effective symmetry; thus, the values presented here serve as a benchmark for the labels' performance in the absence of external structural constraints.

Other design strategies also yield narrow line widths by targeting different sources of broadening. For example, the rigid, two-armed $[Gd(CLaNP13b)]^{3+}$ probe, a chelator based on a central pyridine core, employs a strategy of conformational rigidity.[5] Rather than focusing solely on ligand symmetry to minimize the intrinsic ZFS, it uses two covalent thioether tethers to a protein. This dual-linker approach severely restricts the overall motion and conformational flexibility of the spin label. By minimizing this flexibility, the probe has a reduced ZFS distribution across the ensemble of molecules, which is a primary source of inhomogeneous line broadening, resulting in a narrow central transition with a reported line width of 4.1 mT at 95 GHz.[5]

Similarly, the success of DOTA-based systems as magnetic resonance imaging (MRI) contrast agents is attributed to their structural rigidity. As detailed by Caravan and co-workers,[22] imposing conformational restraints on Gd(III) macrocycles, often through the introduction of sterically demanding substituents, effectively locks the complex into a single, rigid diastereoisomer. In the context of MRI, this conformational locking is crucial for ensuring that the reorientational dynamics of the coordinated water molecule are tightly coupled to the global tumbling of the complex, thereby maximizing relaxivity. In the context of EPR linewdith, the structural rigidity minimizes the inhomogeneity of the ligand field across the frozen ensemble, thus narrowing the observed transition.

https://doi.org/10.1021/acs.inorgchem.6c00631
Inorg. Chem. 2026, 65, 13807−13816

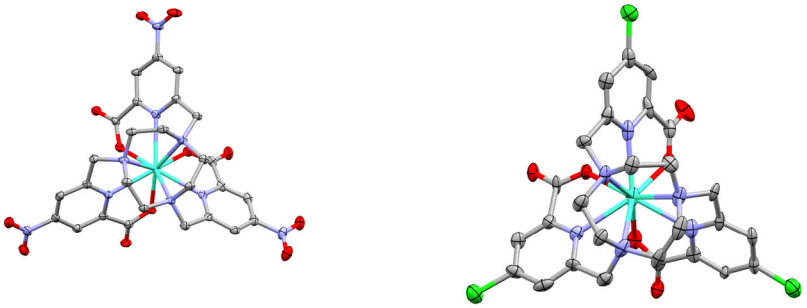

Figure 2. Molecular structures determined by X-ray analysis for [GdL^2] (left) CCDC:2526904 and [GdL^3] (right) CCDC:2526905.

However, even determination of the line width can be an experimental challenge, due to the small ZFS of Gd(III) complexes compared to 3d-block complexes where ZFS can be on the THz scale. Furthermore, while an exceptionally small ZFS is highly desirable for narrowing the central transition and boosting sensitivity, it introduces complications for DEER measurements at short ranges. For Gd(III) tags with small ZFS, distance measurements below ≈3.4 nm suffer from artificial broadening due to the incomplete truncation of the pseudosecular terms in the dipolar Hamiltonian.[23,24] Notably, this artificial broadening is circumvented in electron nuclear double resonance (ENDOR) spectroscopy, where minimized ZFS values remain advantageous for accurate distance determination, therefore the purpose of the tag must be considered when optimizing its structure for either DEER or ENDOR.[25] To fully characterize these parameters, ZFS is usually measured by modeling of EPR spectra with spin Hamiltonian techniques.[26,27]

The total spin Hamiltonian for such molecules is the sum of the ZFS and the Zeeman interactions ($\hat{H} = \hat{H}_{ZFS} + \hat{H}_{Zee}$).[15] At low magnetic fields the ZFS term dominates, but at high magnetic fields the Zeeman term dominates.[15] Hence, for a full determination of the magnetic properties of a probe, both low-field and high-field experiments are required. A key feature of high spin systems is that the central $m_S = -1/2 \leftrightarrow +1/2$ transition is only broadened by ZFS at second order, an effect that is inversely proportional to the applied magnetic field.[13] Consequently, at high spectrometer frequencies (above Q-band, 34 GHz), the second-order broadening is diminished, resulting in a narrow and intense central transition that can be measured with great precision.[15,21] This line-narrowing effect enhances experimental sensitivity, making these compounds ideal for high-resolution distance measurements and efficient polarizing agents for DNP. It is important to acknowledge that while these ligand frameworks are designed to maximize symmetry, conjugation to a protein target will inevitably perturb this geometric ideal. Since each specific labeling site will impose a unique conformational bias, the line widths reported herein represent the intrinsic spectroscopic limits of the free labels.

Herein we study four Gd(III) TPATCN [GdL^{1-4}] and three Gd(III) DOTA [$GdL^{5-7}(H_2O)$] derivatives (Figure 1), designed to minimize ZFS by providing a symmetrical and rigid binding environment, with exceptionally narrow line widths that are strong candidates for next-generation spin labels. We find that electronic functionalization of the TPATCN scaffold is a highly effective strategy for tuning the spectral properties. Specifically, the electron-withdrawing nitro group on [GdL^2] minimizes the axial ZFS parameter, resulting in the smallest $|D|$ value in the series of C_3 molecules at 0.0110 $cm^{-1}\|0.330$ GHz. This, however, is coupled with the largest D_{strain}, suggesting an increase in conformational flexibility. In contrast, the DOTA-based complexes, particularly [$GdL^6(H_2O)]^{3+}$, demonstrate superior structural rigidity and axial symmetry, evidenced by exceptionally small ZFS parameters D, E = 0.0072, 0.000348 $cm^{-1}\|216$, 10.4 MHz. These results reveal a key trade-off between minimizing the intrinsic ZFS magnitude and maintaining high structural homogeneity.

METHODS

Synthesis and Characterization

The synthesis of ligands L^1, L^{4-7} followed literature methods[9,28−30] Details of the synthesis of the ligands L^{2-3} (Figure 2) and their Gd complexes are given in the SI. The complex [GdL^1] was reported earlier by Mazzanti et al.[31]

X-ray Crystallography

Crystalography data was collected using either a Rigaku Oxford Diffraction Synergy-S diffractometer with a dual source equipped with a Hybrid pixel arrary detector or using Kα radiation (λ = 0.71073 Å) on a Bruker D8 V Venture (Photon II 14 detector, IμS 3.0 microfocus sealed tube sources (Cu and Mo) diffractometer) equipped with a Cobra low temperature device. The crystal was kept at 302 or 100 K during data collection. Using Olex2,[32] one structure, [GdL^2], was solved with the ShelXS[33] structure solution program using Direct Methods and refined with ShelXL[34] refinement package using Least Squares minimization. The other crystal, [GdL^3], was solved with olex2.solve[35] structure solution program using Charge Flipping and refined with the olex2.refine[35] refinement package using Gauss−Newton minimization. All non-hydrogen atoms were refined anisotropically; hydrogen atoms were placed in the calculated positions and refined in riding mode. X-ray cyrystal structure images were produced using Mercury CSD 3.6 software using data from the Cambridge Structural Database.

EPR Spectroscopy

Samples were prepared as 2:1 d_6-ethanol:d_4-methanol solutions at 0.1 mM concentration range. Measurements at Q-band (≈34 GHz) were performed with a Bruker Elexsys series spectrometer, equipped with a home-built X-to-Q-band bridge extension compatible with a Bruker ELEXSYS-I X-band EPR spectrometer equipped with a home-built cylindrical resonator.[36] EPR measurements were performed at 10K using an Oxford instruments flexline cryostat. The temperature was held constant using an Oxford Instruments ITC4 temperature controller interfaced to a Lakeshore Cryotonics Cernox thermistor. Samples were quench-cooled by immersion in a cryostat at 10 K, maintained throughout the experiment with an Oxford Instruments helium temperature regulation unit.[4]

Low-Field (Q-Band, 34 GHz) EPR spectra were collected via an electron spin echo (ESE), which is a pulsed EPR experiment as a function of magnetic field, using a two-pulse Hahn echo sequence ($\pi/2-\tau-\pi-\tau-echo$).[37] Longitudinal relaxation times (T_1) were measured using an inversion recovery sequence ($\pi-T-\pi/2-\tau-\pi-\tau-echo$)

https://doi.org/10.1021/acs.inorgchem.6c00631
Inorg. Chem. 2026, 65, 13807−13816

with microwave pulse lengths of $t_{\pi/2}$ = 16 ns and t_{π} = 32 ns. The interpulse delay was fixed at τ = 200 ns, and the inversion recovery delay T was incremented from an initial value of 800 ns.[38] The intensity of the echo was recorded as a function of the variable delay time T. The resulting recovery curve was fitted to a single-exponential function to extract T_1. Phase memory times (T_m) were measured using a Hahn echo decay sequence ($\pi/2{-}\tau{-}\pi{-}\tau{-}echo$) with identical pulse lengths (16/32 ns), an initial τ of 200 ns, and a time step of 4 ns, where the echo intensity was recorded as a function of the interpulse delay τ, and fitted to a stretched-exponential function.[25]

W-Band (94 GHz) EPR spectra for [GdL^2] and [GdL^7] were collected via an ESE as a function of magnetic field. Measurements were performed at 10 K using a modified Bruker E680 spectromter previously described in Nalepa et al.[39] The field-swept spectrum was acquired using a two-pulse Hahn echo sequence ($\pi/2{-}\tau{-}\pi{-}\tau{-}echo$) centered at 3.372 T with a sweep width of 191 mT. The microwave pulse lengths were set to $t_{\pi/2}$ = 40 ns and t_{π} = 80 ns, with a fixed interpulse delay of τ = 500 ns. The same sample mixture as Q-Band was used. Longitudinal relaxation times (T_1) were measured using an inversion recovery sequence ($\pi{-}T{-}\pi/2{-}\tau{-}\pi{-}\tau{-}echo$) with microwave pulse lengths of $t_{\pi/2}$ = 40 ns and t_{π} = 80 ns. The interpulse delay was fixed at τ = 2500 ns, and the inversion recovery delay T was incremented in 200 ns steps. The intensity of the echo was recorded as a function of the variable delay time T, and the resulting recovery curve was fitted to a single-exponential function to extract T_1. Phase memory times (T_m) were measured using a Hahn echo decay sequence ($\pi/2{-}\tau{-}\pi{-}\tau{-}echo$) with identical pulse lengths (40/80 ns), an initial τ of 2500 ns, and a time step of 40 ns. The echo intensity was recorded as a function of the variable interpulse delay τ and fitted to a stretched-exponential function.

For high field EPR, the samples were prepared at a concentration of 1 mM in methanol-d_4 in volumes ranging from 50 to 150 μL in 8 mm diameter polypropylene cups closed with poly(tetrafluoroethylene) caps. Larger volumes were used to increase the sensitivity for some samples. The solvent was degassed by weeks long storage in a fluorinated ethylene propylene (FEP) vial inside a globebox. Indeed, FEP allows O_2 gas to diffuse out overtime leading to increased electron relaxation times, and in this case, leads to narrower EPR lines.[40]

High-field continuous wave (CW) EPR data was recorded at the National High Magnetic Field Laboratory (NHMFL Tallahassee, Florida, USA) utilizing a 15T spectrometer with a set of narrow band frequency sources ranging from 60 to 950 GHz. These sources were purchased from Virginia Diode Inc. (Charlotteville, Virginia, USA). The terahertz signal is transmitted via a series of waveguides and mirrors to an in-house built transmission probe, and the signal is detected with an indium antimonide bolometer purchased from Thomas Keating Ltd. (Billingshurst, United Kingdom). For this work, three select frequencies were used at 120, 240, and 390 GHz. A classic phase-sensitive detection scheme was employed, using a lock-in amplifier to demodulate the EPR signal generated by a modulation coil located around the sample. The temperatures were controlled and set between 5 and 30 K using an Oxford flow cryostat.

Spin Hamiltonian Modeling

A consistent set of spin Hamiltonian parameters was computed for each compound using a multistep approach across the different EPR frequencies using PHI.[27] Spectra were simulated using a spin Hamiltonian including ZFS and Zeeman terms: $\hat{H} = \mu_B \vec{B} \cdot \overline{g} \cdot \hat{S} + D(\hat{S}_z^2 - S(S+1)/3) + E(\hat{S}_x^2 - \hat{S}_y^2)$. Here, $\overline{g}$ is the g-matrix, and D and E are the axial and rhombic ZFS parameters, respectively. Given the exceptionally small magnitude of the g-anisotropy ($\Delta g \approx 10^{-4}$), the principal axes of the g-matrix and the ZFS tensor were assumed to be collinear; introducing relative Euler angles as independent fit parameters would overparameterise the model. To account for structural heterogeneity in the frozen solution, the model also includes strain parameters (g_{strain}, D_{strain}, E_{strain}), which describe Gaussian distributions in the principal Hamiltonian values.[41] Using a fixed Lorentzian line width in frequency space of 0.001 GHz, this effectively means the entire spectral line shape is determined by the strain parameters. The multistep fitting process was designed to reliably decorrelate the ZFS and g-matrix parameters, which can be difficult to uniquely determine with a single spectrum, and to correct for minor, systematic field calibration offsets in the high-field instruments. The procedure was as follows:

1. **Low-field ZFS determination:** The analysis begins with the low-field spectrum (~34 GHz, ~1.1 T), where the spectral line shape is most sensitive to the ZFS parameters. The sharp central feature owing to the $|m_s = 1/2\rangle \leftrightarrow |m_s = -1/2\rangle$ transition is used to fit g_{iso}, and an initial estimate of $g_{iso-strain}$. This was performed using an approximate D parameter to have roughly the correct spectral envelope. Then, the principal ZFS parameters (D, E) and their corresponding strains (D_{strain}, E_{strain}) are fitted in PHI. Note that the spectral simulations are insensitive to the sign of the D parameter, hence it is reported as only the modulus, however the simulations are sensitive to the sign of D/E, and so the relative sign of the E parameter is reported.
2. **High-field correction:** The ZFS and ZFS-strain parameters determined from the low-field fit are then held constant for the analysis of all higher-field spectra (120 GHz, 240 and 390 GHz). To account for systematic offsets in the recorded magnetic field values of the high-field instruments, the experimental spectra were manually shifted along the field axis. This manual alignment corrects for small, systematic inaccuracies (~70 G) in the magnetic field calibration of the high-field instruments, ensuring that the effective g_{iso} value is constant across all frequencies, from the 34 GHz data set.
3. ***g*-matrix anisotropy:** With the experimental data correctly aligned, the anisotropic components of the g-matrix (g_x, g_y, g_z) and their associated strains are then fitted to the shifted high-field data, with fixed ZFS parameters from lower field data. This step is performed independently for each high-field spectrum (4, 8, and 14 T).
4. **Parameter refinement:** The deviations of the fitted anisotropic g-values from the isotropic value ($\Delta g_i = g_i - g_{iso}$, where $i = x, y, z$) are calculated for each high-field data set. The consistency of these Δg values across the different fields is checked to ensure the consistency of the model. A single, unified g-matrix for each complex was then determined by applying the Δg values derived from the highest-resolution, and therefore most precise, data set (typically 390 GHz) to the accurate g_{iso} value determined from the initial 34 GHz fit. The high field calibration values were checked in this final stage also. The final reported parameters and plots reflect this unified model. Explicitly, ZFS and g_{iso} values are established at low-field, and $\Delta g_{x,y,z}$ and their respective strains are discerned at high field.
5. **ZFS strain confidence intervals:** To check the uniqueness of the obtained ZFS strain parameters, we finally survey the error surface of the low-field spectral simulation as a function of D_{strain} and E_{strain} (Figures S8–S13). We use both the numerical least-squares residual error and visual inspection of several points to estimate confidence intervals.

As all measurements were performed on frozen solutions, there is a random distribution of molecular orientations, hence simulations require integrating the magnetic field over a hemisphere of orientations. This numerical hemispherical integration was performed in PHI using the Zaremba-Conroy-Wolfsberg (ZCW) method as described by Eden et al.,[42] an efficient numerical integration scheme for spherical coordinates. A grid of 6765 orientations (corresponding to ZCW level 12 in PHI) was used to ensure accurate and smooth spectral simulations.

Note that spectral simulations were performed using a field-space Lorentzian line width function in PHI following Weihe and Bendix,[43] to be as accurate as possible. However, in this case as we are attempting to find a single unique parameter set across multifrequency data sets, with the ultimate goal being the most reliable model, we note that some discrepancies in the relative intensities between the

https://doi.org/10.1021/acs.inorgchem.6c00631
Inorg. Chem. 2026, 65, 13807−13816

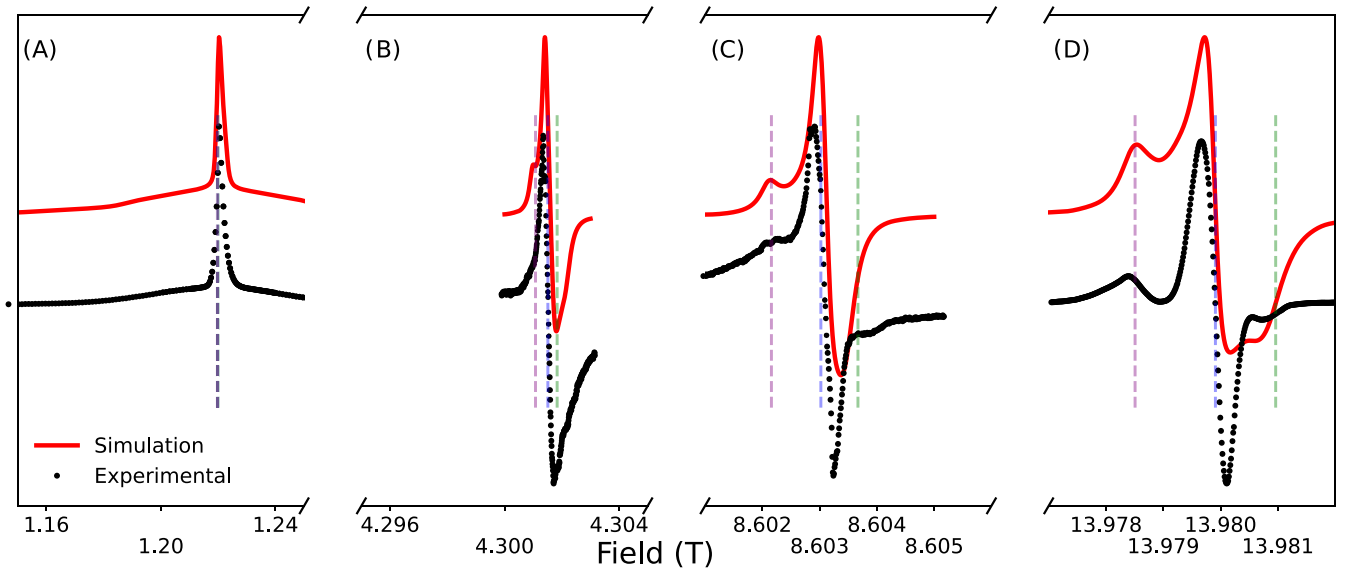

Figure 3. Multifrequency EPR spectra for the [GdL[1]] complex in a frozen solution. Spectra were recorded at (A) 34.04 GHz (10 K), (B) 120 GHz (20 K), (C) 240 GHz (20 K), and (D) 390 GHz (5 K). Experimental data are shown as black traces. The red traces represent the best-fit simulations, where ZFS Hamiltonian parameters are obtained from Q-Band, and *g*-values are obtained from high field to create a single, consistent set of spin Hamiltonian parameters. Three vertical bars across the Field ranges (purple, blue, green) display the consistent g-values that are broadened as a function of field.

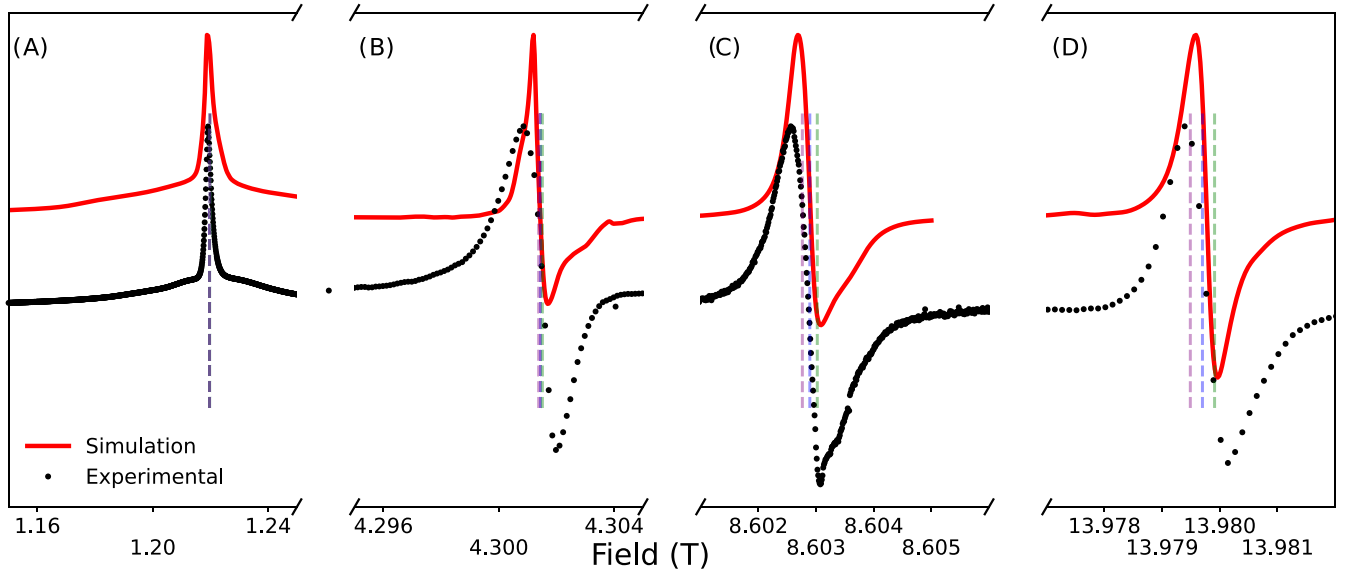

Figure 4. Multifrequency EPR spectra for the $[GdL^5(H_2O)]^-$ complex in a frozen solution. Spectra were recorded at (A) 34.01 GHz (10 K), (B) 120 GHz (5 K), (C) 240 GHz (20 K), and (D) 390 GHz (10 K). Experimental data are shown as black traces. The red traces represent the best-fit simulations, where ZFS Hamiltonian parameters are obtained from Q-Band, and *g*-values are obtained from high field to create a single, consistent set of spin Hamiltonian parameters. Three vertical bars across the field ranges (purple, blue, green) display the consistent g-values that are broadened as a function of field.

experimental and simulated spectra are observed, most notably at the extreme features such as high-field shoulders in the 390 GHz data. Despite these line shape discrepancies, the position of the *g*-features (indicated by the dashed lines) do indeed correspond to the features in the experimental data.

Computational Methods

To complement the experimental spin Hamiltonian parameters, a multistep theoretical protocol was employed to compute the ZFS parameters from first principles.

Geometry Optimization. First, the molecular geometries of all complexes were optimized in the gas phase using density-functional theory (DFT) as implemented in the Gaussian 16 package.[44] The PBE functional[45] was used in conjunction with the cc-pVDZ basis set[46] for all atoms except Gd, where the Stuttgart ECP53MHF f-in-core pseudopotential was used with the corresponding valence basis set.[47] Vibrational frequency calculations were performed at the same level of theory to confirm all optimized structures were true local minima (i.e., possessing no imaginary frequencies).

ZFS and *g*-Matrix Calculations. Using the optimized DFT geometries, the electronic structure and magnetic properties were computed using the OpenMolcas software package.[48] We employed the ANO-RCC-VTZP for the Gd, the ANO-RCC-VDZP for the first coordination sphere atoms, and the ANO-RCC-VDZ basis set for all others.[49−51] State-average complete active space self-consistent field (SA-CASSCF) calculations were performed with an active space of

https://doi.org/10.1021/acs.inorgchem.6c00631
Inorg. Chem. 2026, 65, 13807−13816

Table 1. Fitted g-Matrix Parameters for the Gd(III) Complexes

compound	g_x	$g_{x,strain}$	g_y	$g_{y,strain}$	g_z	$g_{z,strain}$
[GdL^1]	1.99319	0.00006	1.99304	0.00012	1.99339	0.00009
[GdL^2]	1.99335	0.00007	1.99318	0.00006	1.99304	0.00027
[GdL^3]	1.99329	0.00006	1.99317	0.000556	1.99335	0.000064
[GdL^4]$^{3-}$	1.99293[a]	0.0002	1.99313[a]	0.00006	1.99403[a]	0.0004
[GdL^5(H$_2$O)]$^-$	1.99322	0.0003	1.99319	0.00008	1.99325	0.00008
[GdL^6(H$_2$O)]$^{3+}$	1.9929	0.0005	1.9928	0.0003	1.9926	0.0006
[GdL^7(H$_2$O)]$^{3+}$	1.99193[b]	0.0002	1.99199[b]	0.0002	1.9919[b]	0.0004

[a]The g_{iso} was fixed to the average of [GdL^1], [GdL^2] and [GdL^3]. [b]The g_{iso} was extracted from W-band data. We note here that the precision in anisotropic g-values is well-defined at high-field. That said we acknowledge that the accuracy of isotropic g-values is limited to ±0.0005 due to instrumentation limitations. The principal axes (x, y, z) are defined by the zero-field splitting tensor. The variation in the ordering of the largest g-value simply reflects its orientation relative to the primary ZFS axis in the molecular frame.

seven 4f electrons in seven 4f orbitals. To accurately compute the ZFS, all 21 sextet spin states were included, along with the ground octet state, which were mixed by spin−orbit coupling. The static ZFS parameters (D and E) and principal components of the g-matrix were extracted using the Single_Aniso module.[52]

RESULTS AND DISCUSSION

Following the methodology outlined above, we collected variable frequency EPR spectra for the compounds in Figure 1. The multifrequency approach provides a systematic way to decorrelate and precisely determine all spin Hamiltonian parameters. This is because, at Q- or W-band (∼1 or ∼3 T), the spectral line shape is dominated by the ZFS and its overall breadth provides a robust measure of the magnitude of the axial (|D|) and rhombic (E) parameters. Moving to progressively higher fields (120, 240, and 390 GHz), the Zeeman interaction becomes dominant and the data emphasizes the ±1/2 transition, causing spectral features to become highly sensitive to the small g-anisotropy. This allows for the precise resolution of the individual components of the g-matrix (g_x, g_y, g_z), and their respective strains, which are not observable at lower fields.

However, owing to limitations in signal intensity and instrument availability, complete multifrequency data sets could not be obtained for all seven compounds. For compound [GdL^4]$^{3-}$, which is lacking Q- and W-band data, we have fixed the reported D value from Maity et al.[13] and focused on obtained anisotropic g values and their strains. For [GdL^7(H$_2$O)]$^{3+}$, ZFS parameters were estimated using W-band data instead of Q-band data. To verify that W-band contains intrinsically the same information as Q-band, we also measured the W-band spectrum for the well-characterized GdL^2 complex, which showed excellent agreement between Q-band and W-band derived parameters S2.

We will first discuss the spectral profiles of [GdL^1](Figure 3) which are representative of the other compounds herein (Figures 4 and S1−S6). The 34 GHz ESE spectrum appears as a sharp central line, corresponding to the m_S = −1/2 ↔ +1/2 transition, with smooth "wings" arising from the other Δm_S = ±1 transitions; the latter are affected at first order by the ZFS, and so appear broadened. Hence, at low field we can accurately model the spectrum to obtain good estimates of the ZFS parameters, and here, where we have precise knowledge of the microwave frequency and magnetic field, we can accurately determine the isotropic g-value. The high-frequency data are recorded in continuous wave mode with field modulation, and so appear as first-derivative spectra. At the higher frequency, we observe more structure to the data than at low frequency. At 240 and 390 GHz, for the field ranges captured here, we only observe the m_S = −1/2 ↔ +1/2 transition, and so the structure results from the g-anisotropy. For [GdL^1], in this case we can directly resolve the largest g-value as a bump at lower magnetic field; however this is not clearly observable for all compounds herein due to larger g-strain. Following the methodology in the Methods section provides a robust method of refining the large number of model parameters.

Fitting the spectra for each compound as described, we find isotropic g-values all being approximately 1.993 (Table 1), consistent with the expected value for the orbitally non-degenerate $^8S_{7/2}$ ground state of Gd(III), which has a negligible orbital contribution to its magnetic moment.[13,15]

Regarding the ZFS values along the TPATCN series (Table 2), we observe an electronic trend. The complexes substituted

Table 2. Zero-Field Splitting (ZFS) Parameters for the Gd(III) Complexes[c]

compound	|D|	D_{strain}	E	E_{strain}
[GdL^1]	0.0153	0.004(1)	−0.0051	0.001(1)
[GdL^2]	0.0110	0.015(5)	0.00331	0.004(2)
[GdL^3]	0.0138	0.008(3)	0.00455	0.015(10)
[GdL^4]$^{3-}$	0.0162[a]	0.009[a]	0[a]	0[a]
[GdL^5(H$_2$O)]$^-$	0.0216	0.010(1)	−0.00648	0.001(1)
[GdL^6(H$_2$O)]$^{3+}$	0.0072	0.003(1)	0.000348	0.001(1)
[GdL^7(H$_2$O)]$^{3+}$	0.0055[b]	0.003(1)[b]	−0.0018[b]	0.001(1)[b]

[a]Lacking low-field data, the D value for [GdL^4]$^{3-}$ is fixed from literature,[13] E and E_{strain} are fixed to zero, and D_{strain} is fixed to the average of [GdL^1], [GdL^2] and [GdL^3]. [b]For [GdL^7(H$_2$O)]$^{3+}$, ZFS parameters were derived from W-band measurements. [c]Values are given in cm^{-1}. Estimated confidence intervals for ZFS strain are given in parentheses.

with electron-withdrawing groups, i.e., the nitro- ([GdL^2]) and chloro- ([GdL^3]) derivatives, have smaller axial ZFS values (|D| ≈ 0.011−0.014 cm^{-1}‖0.33−0.42 GHz) than the parent complex [GdL^1]. Conversely, [GdL^4]$^{3-}$ with its electron-donating thio-acid substituents appears to have a larger ZFS, rising to |D| ≈ 0.016 cm^{-1}‖0.485 GHz based on the report from Maity et al.[13]

For the DOTA-derived series, we observe that the axial ZFS for the parent DOTA complex [GdL^5(H$_2$O)]$^-$ is significantly larger than for the amide-substituted derivatives [GdL^6(H$_2$O)]$^{3+}$ and [GdL^7(H$_2$O)]$^{3+}$. This implies that the primary amide derivatives possess particularly symmetric coordination geometries, effectively minimizing the axial ZFS compared to the parent DOTA by restricting the flexibility of the pendant arms. All complexes maintain high axial symmetry, with |E| values well below the rhombic limit (E/D = 1/3).

https://doi.org/10.1021/acs.inorgchem.6c00631
Inorg. Chem. 2026, 65, 13807−13816

In terms of the ZFS strain parameters (D_{strain} and E_{strain}), the only main observation across all data collected herein is that the largest strains are observed for [GdL^2] and [GdL^5(H$_2$O)]$^-$. These compounds are the ones with the most polarized exposed functional groups (viz. nitro- and carboxy-, respectively), compared to the other compounds in their respective series. We suspect that this increases inhomogeneity in the coordination environment across the frozen ensemble.

Regarding the absolute magnitude of the ZFS parameters observed in these two series, they compare favorably with other widely used Gd(III) spin labels. For instance, the common [Gd(PyMTA)]$^-$ complex exhibits a significantly larger axial ZFS of $|D| \approx 0.056$ cm^{-1}‖1.68 GHz.[18] Smaller ZFS parameters translate to narrower spectral lines. Using the peak-to-peak line width, ΔB_{pp} (FWHM $\approx \sqrt{3} \times \Delta B_{pp}$) convention,[53] early Gd-DOTA labels showed a width of ∼0.52 mT at 240 GHz.[21] Similarly, the rigid [Gd(CLaNP13b)]$^{3+}$ tag has an estimated ΔB_{pp} of 0.64 mT at 95 GHz,[5] and the CLaNP-5 tag typically exhibits a width of ∼1.2 mT at 34 GHz, while the widely used [Gd-PyMTA]$^-$ label shows line widths in the range of 0.5−1.0 mT at 34 GHz.

The exceptionally small intrinsic ZFS and strain of the complexes studied herein lead to narrow lines: we observe ΔB_{pp} values of 0.8 mT and 0.6 mT for [GdL^2] and [GdL^6(H$_2$O)]$^{3+}$, respectively, at ∼34 GHz (Table S1). These values represent a significant improvement over state-of-the-art labels at Q-band and are competitive with the resolution of current dual-linker strategies often limited by residual conformational flexibility.[54]

Turning to the high-field data, the multifrequency approach allows for the resolution of the individual principal components of the *g*-matrix and their associated strains (Table 1). Consistent with the orbitally nondegenerate $^8S_{7/2}$ ground state of the Gd(III) ion, all complexes exhibit isotropic *g*-values rounding to 1.993, with the exception of [GdL^7(H2O)]$^{3+}$ ($g_{iso} \approx 1.992$). This minor discrepancy is attributed to its measurement at W-band which uses a superconducting magnet as opposed to the electromagnet at Q-band, that may have a slight offset that shifts the apparent *g*-value. The deviations from the free-electron *g*-value and the overall anisotropies are exceedingly small, confirming the high symmetry of the ligand fields. Within the TPATCN series, the parent [GdL^1] and the electron-withdrawing derivatives [GdL^2] and [GdL^3] display tight *g*-matrix clustering (1.9930−1.9934) and minimal *g*-strain (≈10^{-4}). The introduction of electron-donating groups subtly shifts these values; the bulky thio-acid derivative [GdL^4]$^{3-}$ elevates the principal components to ≈1.99336.

For the DOTA series, the parent macrocycle [GdL^5(H$_2$O)]$^-$ maintains a highly isotropic *g*-matrix (1.99319−1.99325) with similarly low strain. Altering the pendant arms from carboxylates to primary amides in [GdL^6(H$_2$O)]$^{3+}$ induces a slight shift to lower *g*-values (1.9926−1.9929). Further adding bulk to the DOTA macrocycle, particularly ethyl groups on [GdL^7(H$_2$O)]$^{3+}$ increase the anisotropy in *g*. Ultimately, the magnitude of the *g*-anisotropy remains minimal across both series, demonstrating that the structural and electronic modifications primarily manifest as changes to the zero-field splitting rather than the *g*-matrix though the permutations in structure give logical repercussions to the *g*-values.

Along with determination of ZFS and *g*-values, we have measured spin−lattice (or longitudinal, T_1) and phase memory (or transverse, T_m) relaxation times (Table 3) at 10 K at 34 GHz.

Table 3. Spin−Lattice (T_1) and Phase Memory (T_m) Relaxation Times for the Gd(III) Complexes, Measured at 10 K and 34 GHz[a]

sample	T_1 (μs)	α_{T_1}	T_m (μs)	α_{T_m}
[GdL^1]	66	0.689	7.56	0.856
[GdL^2]	59	0.686	6.92	0.813
[GdL^3]	58	0.696	4.00	0.839
[GdL^5(H$_2$O)]$^-$	29.9	0.688	5.48	0.893
[GdL^7(H$_2$O)]$^{3+}$	17.5	0.792	5.14	0.901

[a]The T_1 data were fitted to a stretched exponential recovery function of the form $I(t) = I_0(1 - \exp[-(t/T_1)^\alpha])$, while the T_m data were fitted to a stretched exponential decay of the form $I(2\tau) = I_0 \exp[-((2\tau)/T_m)^\alpha]$, where α is the stretching factor $\alpha \leq 1$.

The relaxation behavior across the two series is relatively consistent, with T_1 values ranging from approximately 17 to 66 μs and T_m values generally falling between 4 and 8 μs (Figure S7). We observe that complexes capable of excluding solvent water from the immediate environment of the Gd(III) ion exhibit significantly prolonged relaxation times. Within the TPATCN series, the parent [GdL^1] and its substituted analogues ([GdL^2], [GdL^3]) exhibit comparable relaxation rates ($T_1 \approx 60$ μs; $T_m \approx 4-7$ μs), indicating that the electronic nature of the ring substituent has a minimal impact on the relaxation dynamics at this temperature. In the DOTA series, the relaxation times are notably shorter, with the parent [GdL^5(H$_2$O)]$^-$ showing $T_1 \approx 30$ μs and $T_m \approx 5$ μs, and its derivatives even less so ($T_1 = 17.5$, $T_2 = 5.14$). This reduction compared to the TPATCN series likely reflects differences in the hydration state ($q = 1$ for DOTA vs $q = 0$ for TPATCN) and the solvent accessibility of the metal center. While no single complex in this study exhibits exceptionally long phase memory times typically associated with highly shielded environments, the values are sufficient for standard pulsed EPR applications.

In an attempt to further rationalize our experimental observations on ZFS values and their strains, we have performed *ab initio* calculations of the ZFS tensor. Briefly, this involves gas-phase geometry optimization with density-functional theory (DFT) and then calculation of ground and excited electronic states with multiconfigurational complete active space self-consistent field spin−orbit (CASSCF-SO) methods (see Methods section for details). These calculations predict ZFS on the correct order of magnitude as determined experimentally (Figure 5), but show poor absolute agreement and do not predict the trends. However, if we include the ZFS strain parameters as "error bars" on the plot (note that they are not errors, they are distributions), we observe that the *ab initio* values are within the expected conformational space. When the strain on *D* or *E* is large, there are regions of those distributions where the convention of $E/D \leq 1/3$ is not obeyed, and in order to follow convention would require a redefinition of the axis system, thereby rediagonalizing the ZFS matrix for a new set of results in accord with convention. Effectively this implies that a large horizontal or vertical error bar could be switched into a vertical or horizontal bar, respectively.

As such, the computational predictions are within the area of feasibility. The geometric structure—electronic structure relationship in both TPATCN and DOTA derivatives is

https://doi.org/10.1021/acs.inorgchem.6c00631
Inorg. Chem. 2026, 65, 13807−13816

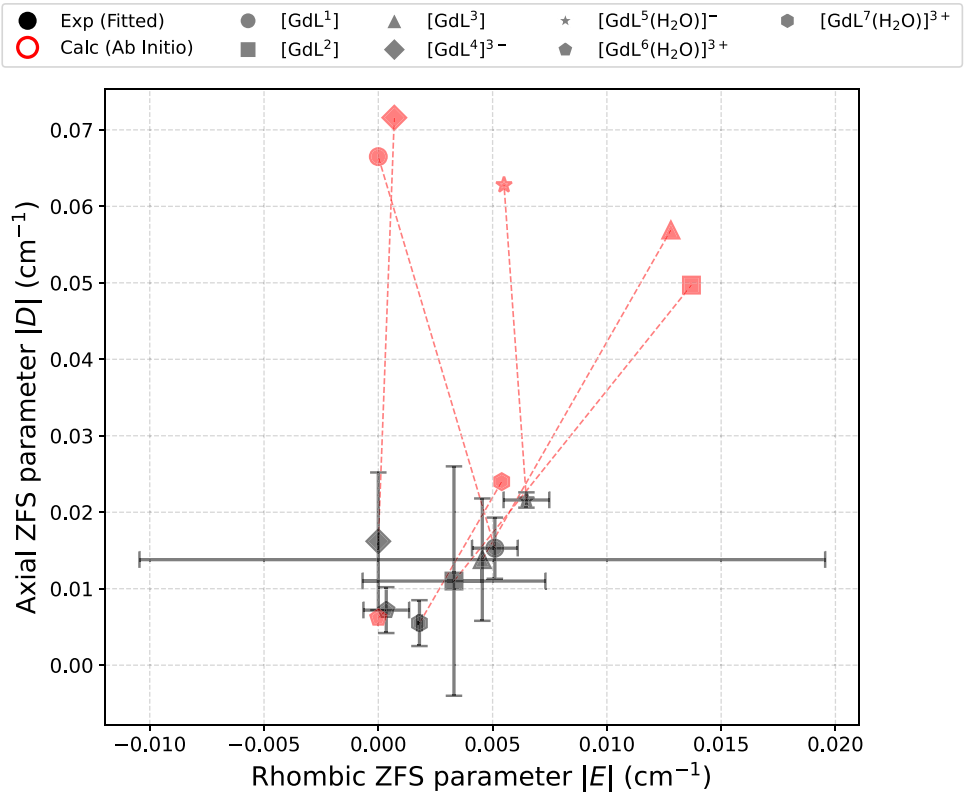

Figure 5. Comparison of experimental (fitted) and theoretical (*ab initio*) spin Hamiltonian parameters. The plot shows the axial ZFS parameter, D, versus the magnitude of the rhombic ZFS parameter, $|E|$ (both in cm^{-1}). Experimental values derived from the global fit of the multifrequency EPR spectra are shown in black with strain values added as error bars, while the static parameters computed *ab initio* are shown in red. Each shape corresponds to a different Gd(III) complex, as indicated in the legend, visually representing the agreement between experiment and theory. Finally, the dashed red lines link *ab initio* and experimental values of respective molecules.

notoriously sensitive. Many experimental and theoretical works have been devoted to this feature for other trivalent lanthanides ions outside of Gd(III).[28−30,55−62] The strong structural sensitivity toward ZFS is borne out experimentally by the observation that often the strain parameters are larger than the central ZFS parameters. This was previously observed in the solid-state EPR spectra of $[LnL^1]$ complexes,[29] and a similar effect on the sensitivity of magnetic anisotropy in the solid state for $[LnL^5(H_2O)]^-$ complexes.[56] Should more computational time be devoted to linear vibronic coupling models,[63] we expect the ensemble of structures would encompass the respective experimental values gathered in this report (Table 2).

Finally, as a general point, it is very difficult to calculate spectral quantities on this tiny energy scale (<0.1 cm^{-1}): for comparison, "chemical accuracy" in quantum chemistry is usually taken as 1 kcal/mol, which is ∼350 cm^{-1}‖10.5 GHz—three orders of magnitude larger than our energy scale here.

CONCLUSION

In this work, we have performed a comprehensive experimental investigation of a series of C_3-symmetric TPATCN and C_4-macrocyclic DOTA-based Gd(III) complexes in an attempt to find structure−property relationships for the rational design of new spin labels. We find that within the TPATCN series there is a trend of electron-withdrawing substituents decreasing the ZFS. In the more flexible DOTA series, we observe that the more-bulky substituted ligands tend to have smaller ZFS, suggesting a higher-symmetry coordination environment. In both series, we find that exposed highly polarized groups lead to larger strain, i.e., distributions, in the ZFS parameters, suggesting larger conformational heterogeneity in the ensembles. We postulate that this derives from greater hydrogen bonding with the solvent matrix.

While minimizing the hydrophilicity of the ligand could theoretically reduce the strain and lead to narrower line widths, practical applications in DEER spectroscopy demand high aqueous solubility. Therefore, the optimal strategy for next-generation spin labels must focus on a middle ground between hydrophilicity and narrow line width.

Using either the TPATCN or DOTA scaffolds, the present line widths are significantly smaller than contemporary spin labels, showing there is considerable scope for the design of next-generation Gd(III) labels with narrower line widths for application in DEER, DNP & SDSL.

ASSOCIATED CONTENT

Data Availability Statement

Research data is available at 10.5281/zenodo.18452147.

Supporting Information

The Supporting Information is available free of charge at https://pubs.acs.org/doi/10.1021/acs.inorgchem.6c00631.

Synthetic procedures, compound characterization, and supplementary EPR spectra for complexes $[GdL^{1-7}]$ (PDF)

https://doi.org/10.1021/acs.inorgchem.6c00631
Inorg. Chem. 2026, 65, 13807−13816

Accession Codes

Deposition Numbers 2526904−2526905 contain the supplementary crystallographic data for this paper. These data can be obtained free of charge via the joint Cambridge Crystallographic Data Centre (CCDC) and Fachinformationszentrum Karlsruhe Access Structures service.

AUTHOR INFORMATION

Corresponding Author

Nicholas F. Chilton − *Research School of Chemistry, Canberra 2601, Australia; Department of Chemistry, The University of Manchester, Manchester M13 9PL, United Kingdom;* orcid.org/0000-0002-8604-0171; Email: nicholas.chilton@anu.edu.au

Authors

Edward Latham − *Research School of Chemistry, Canberra 2601, Australia*

Chowan Ashok Kumar − *Department of Chemistry, Hong Kong Baptist University, Kowloon Tong, Hong Kong 999077, China;* orcid.org/0000-0003-0124-8596

Carlson Alexander − *Department of Chemistry, Hong Kong Baptist University, Kowloon Tong, Hong Kong 999077, China;* orcid.org/0000-0003-4287-2862

Nicholas Cox − *Research School of Chemistry, Canberra 2601, Australia;* orcid.org/0000-0002-7815-6115

Thierry Dubroca − *National High Magnetic Field Laboratory, Tallahassee, Florida 32310-370, United States*

David Parker − *Department of Chemistry, Hong Kong Baptist University, Kowloon Tong, Hong Kong 999077, China; Department of Chemistry, Durham University, Durham DH1 3LE, United Kingdom*

Complete contact information is available at: https://pubs.acs.org/10.1021/acs.inorgchem.6c00631

Notes

The authors declare no competing financial interest.

ACKNOWLEDGMENTS

We thank the Australian National University for providing the resources and support necessary for this research. N.C. thanks the ARC for funding (DP240100273). D.P. thanks the Hong Kong Jockey Club Charities Trust for equipment support and the Hong Kong Government and Hong Kong Baptist University for support under the Global STEM Professorship scheme. We thank Max Les for preparing samples prior to Q-Band measurements. The National High Magnetic Field Laboratory is funded by the National Science Foundation (DMR-2128556) and the State of Florida.

REFERENCES

(1) Fanucci, G. E.; Cafiso, D. S. *Curr. Opin. Struct. Biol.* **2006**, *16*, 644−653.

(2) Jeschke, G. *Annu. Rev. Phys. Chem.* **2012**, *63*, 419−446.

(3) Ardavan, A.; Bowen, A. M.; Fernandez, A.; Fielding, A. J.; Kaminski, D.; Moro, F.; Muryn, C. A.; Wise, M. D.; Ruggi, A.; McInnes, E. J.; et al. *npj Quantum Inf.* **2015**, *1*, No. 15012.

(4) Pierro, A.; Bonucci, A.; Normanno, D.; Ansaldi, M.; Pilet, E.; Ouari, O.; Guigliarelli, B.; Etienne, E.; Gerbaud, G.; Magalon, A.; et al. *Chem. - Eur J* **2022**, *28*, No. e202202249.

(5) Miao, Q.; Zurlo, E.; de Bruin, D.; Wondergem, J. A.; Timmer, M.; Blok, A.; Heinrich, D.; Overhand, M.; Huber, M.; Ubbink, M. *Chem. - Eur. J.* **2020**, *26*, 17128−17133.

(6) Plainchont, B.; Berruyer, P.; Dumez, J.-N.; Jannin, S.; Giraud, N. *Analyst* **2018**, *143*, 3526−3540.

(7) Corzilius, B. *Annu. Rev. Phys. Chem.* **2020**, *71*, 143−170.

(8) Kucher, S.; Elsner, C.; Safonova, M.; Maffini, S.; Bordignon, E. *J. Phys. Chem. Lett.* **2021**, *12*, 3679−3684.

(9) Shah, A.; Starck, M.; Roux, A.; Mosely, J. A.; Stevens, M.; Norman, D. G.; Hunter, R. I.; Mkami, H. E.; Smith, G. M.; Parker, D.; Lovett, J. E. *Inorg. Chem.* **2019**, *58*, 3015−3025.

(10) Matalon, E.; Huber, T.; Hagelueken, G.; Graham, B.; Frydman, V.; Feintuch, A.; Otting, G.; Goldfarb, D. *Angew. Chem., Int. Ed.* **2013**, *52*, 11831−11834.

(11) Yang, Y.; Yang, F.; Gong, Y.-J.; Bahrenberg, T.; Feintuch, A.; Su, X.-C.; Goldfarb, D. *J. Phys. Chem. Lett.* **2018**, *9*, 6119−6123.

(12) Yang, Y.; Yang, F.; Li, X.-Y.; Su, X.-C.; Goldfarb, D. *J. Phys. Chem. B* **2019**, *123*, 1050−1059.

(13) Maity, S.; Price, B. D.; Wilson, C. B.; Mukherjee, A.; Starck, M.; Parker, D.; Wilson, M. Z.; Lovett, J. E.; Han, S.; Sherwin, M. S. *Angew. Chem., Int. Ed.* **2023**, *62*, No. e202212832.

(14) Garbuio, L.; Zimmermann, K.; Häussinger, D.; Yulikov, M. *J. Magn. Reson.* **2015**, *259*, 163−173.

(15) Dubroca, T.; Wang, X.; Mentink-Vigier, F.; Trociewitz, B.; Starck, M.; Parker, D.; Sherwin, M. S.; Hill, S.; Krzystek, J. *J. Magn. Reson.* **2023**, *353*, No. 107480.

(16) Abragam, A.; Bleaney, B. *Electron Paramagnetic Resonance of Transition Ions*; Clarendon Press: 1970.

(17) Rudowicz, C.; Misra, S. K. *Appl. Spectrosc. Rev.* **2001**, *36*, 11−63.

(18) Clayton, J. A.; Keller, K.; Qi, M.; Wegner, J.; Koch, V.; Hintz, H.; Godt, A.; Han, S.; Jeschke, G.; Sherwin, M. S.; et al. *Phys. Chem. Chem. Phys.* **2018**, *20*, 10470−10492.

(19) Khan, S. Zero-Field Splitting in Gd (III) complexes: Towards a molecular understanding of paramagnetic relaxation; Ph. D. Thesis, Stockholm University, 2016.

(20) Neese, F. *WIREs Comput. Mol. Sci.* **2012**, *2*, 73−78.

(21) Raitsimring, A. M.; Gunanathan, C.; Potapov, A.; Efremenko, I.; Martin, J. M.; Milstein, D.; Goldfarb, D. *J. Am. Chem. Soc.* **2007**, *129*, 14138−14139.

(22) Caravan, P. *Chem. Soc. Rev.* **2006**, *35*, 512−523.

(23) Dalaloyan, A.; Qi, M.; Ruthstein, S.; Vega, S.; Godt, A.; Goldfarb, D. *Phys. Chem. Chem. Phys.* **2015**, *17*, 18464−18476.

(24) Cohen, M. R.; Frydman, V.; Milko, P.; Iron, M. A.; Godt, A.; Goldfarb, D. *Phys. Chem. Chem. Phys.* **2016**, *18*, 12847−12854.

(25) Judd, M.; Qi, M.; Abdelkader, E. H.; Qianzhu, H.; Savitsky, A.; Huber, T.; Harmer, J. R.; Godt, A.; Otting, G.; Cox, N. *J. Am. Chem. Soc.* **2025**, *147*, 16826−16835.

(26) Stoll, S.; Schweiger, A. *J. Magn. Reson.* **2006**, *178*, 42−55.

(27) Chilton, N. F.; Anderson, R. P.; Turner, L. D.; Soncini, A.; Murray, K. S. *J. Comput. Chem.* **2013**, *34*, 1164−1175.

(28) Vonci, M.; Mason, K.; Suturina, E. A.; Frawley, A. T.; Worswick, S. G.; Kuprov, I.; Parker, D.; McInnes, E. J. L.; Chilton, N. F. *J. Am. Chem. Soc.* **2017**, *139*, 14166−14172.

(29) Vonci, M.; Mason, K.; Neil, E. R.; Yufit, D. S.; McInnes, E. J. L.; Parker, D.; Chilton, N. F. *Inorg. Chem.* **2019**, *58*, 5733−5745.

(30) Mason, K.; Harnden, A. C.; Patrick, C. W.; Poh, A. W. J.; Batsanov, A. S.; Suturina, E. A.; Vonci, M.; McInnes, E. J. L.; Chilton, N. F.; Parker, D. *Chem. Commun.* **2018**, *54*, 8486−8489.

(31) Gateau, C.; Mazzanti, M.; Pécaut, J.; Dunand, F. A.; Helm, L. *Dalton Trans.* **2003**, *4*, 2428−2433.

(32) Dolomanov, O. V.; Bourhis, L. J.; Gildea, R. J.; Howard, J. A. K.; Puschmann, H. *J. Appl. Crystallogr.* **2009**, *42*, 339−341.

(33) Sheldrick, G. M. *Acta Crystallogr., Sect. A:Found. Crystallogr.* **2008**, *64*, 112−122.

(34) Sheldrick, G. M. *Acta Crystallogr., Sect. A:Found. Adv.* **2015**, *71*, 3−8.

(35) Bourhis, L. J.; Dolomanov, O. V.; Gildea, R. J.; Howard, J. A.; Puschmann, H. *Acta Crystallogr., Sect. A:Found. Adv.* **2015**, *71*, 59−75.

(36) Judd, M.; Jolley, G.; Suter, D.; Cox, N.; Savitsky, A. *Appl. Magn. Reson.* **2022**, *53*, 963−977.

(37) Hahn, E. L. *Phys. Rev.* **1950**, *80*, No. 580.

(38) Schweiger, A.; Jeschke, G. *Principles of Pulse Electron Paramagnetic Resonance*; Oxford University Press, 2001.
(39) Nalepa, A.; Möbius, K.; Lubitz, W.; Savitsky, A. *J. Magn. Reson.* **2014**, *242*, 203−213.
(40) Quan, Y.; Subramanya, M. V. H.; Ouyang, Y.; Mardini, M.; Dubroca, T.; Hill, S.; Griffin, R. G. *J. Phys. Chem. Lett.* **2023**, *14*, 4748−4753.
(41) Chilton, N. F. *PHI User Manual v3* 2023.
(42) Eden, M.; Levitt, M. H. *J. Magn. Reson.* **1998**, *132*, 220−239.
(43) Husein Mor, H.; Weihe, H.; Bendix, J. *J. Magn. Reson.* **2010**, *207*, 283−286.
(44) Frisch, M. J.; Trucks, G. W.; Schlegel, H. B.; Scuseria, G. E.; Robb, M. A.; Cheeseman, J. R.; Scalmani, G.; Barone, V.; Petersson, G. A.; Nakatsuji, H.; Li, X.; Caricato, M.; Marenich, A. V.; Bloino, J.; Janesko, B. G.; Gomperts, R.; Mennucci, B.; Hratchian, H. P.; Ortiz, J. V.; Izmaylov, A. F.; Sonnenberg, J. L.; Williams-Young, D.; Ding, F.; Lipparini, F.; Egidi, F.; Goings, J.; Peng, B.; Petrone, A.; Henderson, T.; Ranasinghe, D.; Zakrzewski, V. G.; Gao, J.; Rega, N.; Zheng, G.; Liang, W.; Hada, M.; Ehara, M.; Toyota, K.; Fukuda, R.; Hasegawa, J.; Ishida, M.; Nakajima, T.; Honda, Y.; Kitao, O.; Nakai, H.; Vreven, T.; Throssell, K.; Montgomery, J. A., Jr.; Peralta, J. E.; Ogliaro, F.; Bearpark, M. J.; Heyd, J. J.; Brothers, E. N.; Kudin, K. N.; Staroverov, V. N.; Keith, T. A.; Kobayashi, R.; Normand, J.; Raghavachari, K.; Rendell, A. P.; Burant, J. C.; Iyengar, S. S.; Tomasi, J.; Cossi, M.; Millam, J. M.; Klene, M.; Adamo, C.; Cammi, R.; Ochterski, J. W.; Martin, R. L.; Morokuma, K.; Farkas, O.; Foresman, J. B.; Fox, D. J. *Gaussian 16, Revision C.01*; Gaussian, Inc.: Wallingford CT, 2016.
(45) Perdew, J. P.; Burke, K.; Ernzerhof, M. *Phys. Rev. Lett.* **1996**, *77*, No. 3865.
(46) Dunning, T. H. *J. Chem. Phys.* **1989**, *90*, 1007−1023.
(47) Dolg, M.; Stoll, H.; Savin, A.; Preuss, H. *Theor. Chim. Acta* **1989**, *75*, 173−194.
(48) Galv'an, I. F.; Vacher, M.; Alavi, A.; Angeli, C.; Aquilante, F.; Autschbach, J.; Bao, J. J.; Bokarev, S. I.; Bogdanov, N. A.; Carlson, R. K.; et al. *J. Chem. Theory Comput.* **2019**, *15*, 5925−5964.
(49) Roos, B. O.; Lindh, R.; Malmqvist, P.-Å.; Veryazov, V.; Widmark, P.-O. *J. Phys. Chem. A* **2004**, *108*, 2851−2858.
(50) Roos, B. O.; Lindh, R.; Malmqvist, P.-Å.; Veryazov, V.; Widmark, P.-O. *Chem. Phys. Lett.* **2005**, *409*, 295−299.
(51) Roos, B. O.; Lindh, R.; Malmqvist, P.-Å.; Veryazov, V.; Widmark, P.-O. *J. Phys. Chem. A* **2005**, *109*, 6575−6579.
(52) Chibotaru, L. F.; Ungur, L. *J. Chem. Phys.* **2012**, *137*, No. 064112.
(53) Poole, C. P. *Electron Spin Resonance: A Comprehensive Treatise on Experimental Techniques*, 2nd ed.; John Wiley and Sons: New York, 1983.
(54) Palit, S.; Hasanbasri, Z.; Moriglioni, N. A.; Casto, J.; Saxena, S. *J. Phys. Chem. Lett.* **2025**, *16*, 10256−10264.
(55) Boulon, M. E.; Cucinotta, G.; Luzon, J.; Degl'Innocenti, C.; Perfetti, M.; Bernot, K.; Calvez, G.; Caneschi, A.; Sessoli, R. *Angew. Chem., Int. Ed.* **2013**, *125*, 368−372.
(56) Cucinotta, G.; Perfetti, M.; Luzon, J.; Etienne, M.; Car, P.; Caneschi, A.; Calvez, G.; Bernot, K.; Sessoli, R. *Angew. Chem., Int. Ed.* **2012**, *51*, 1606−1610.
(57) Briganti, M.; Garcia, G. F.; Jung, J.; Sessoli, R.; Guennic, B. L.; Totti, F. *Chem. Sci.* **2019**, *10*, 7233−7245.
(58) Chilton, N. F.; Collison, D.; McInnes, E. J. L.; Winpenny, R. E. P.; Soncini, A. *Nat. Commun.* **2013**, *4*, No. 2551.
(59) Harnden, A. C.; Suturina, E. A.; Batsanov, A. S.; Senanayake, P. K.; Fox, M. A.; Mason, K.; Vonci, M.; McInnes, E. J. L.; Chilton, N. F.; Parker, D. *Angew. Chem., Int. Ed.* **2019**, *58*, 10290−10294.
(60) Suturina, E. A.; Mason, K.; Botta, M.; Carniato, F.; Kuprov, I.; Chilton, N. F.; McInnes, E. J. L.; Vonci, M.; Parker, D. *Dalton Trans.* **2019**, *48*, 8400−8409.
(61) Manvell, A. S.; Pfleger, R.; Bonde, N. A.; Briganti, M.; Mattei, C. A.; Nannestad, T. B.; Weihe, H.; Powell, A. K.; Ollivier, J.; Bendix, J.; Perfetti, M. *Chem. Sci.* **2023**, *15*, 113−123.
(62) Waldmann, O. A. *J. Am. Chem. Soc.* **2026**, *148*, 50−54.
(63) Staab, J. K.; Chilton, N. F. *J. Chem. Theory Comput.* **2022**, *18*, 6588−6599.

https://doi.org/10.1021/acs.inorgchem.6c00631
Inorg. Chem. 2026, 65, 13807−13816